Sustainable Energy & Fuels

ROYAL SOCIETY OF CHEMISTRY

PAPER

View Article Online
View Journal | View Issue

Cite this: *Sustainable Energy Fuels*, 2023, **7**, 5066

Analysis of charge trapping and long lived hole generation in $SrTiO_3$ photoanodes†

Anna A. Wilson, [a] Thomas P. Shalvey,[b] Andreas Kafizas, [ac] Asim Mumtaz[bd] and James R. Durrant *[ae]

Received 10th July 2023
Accepted 1st September 2023

DOI: 10.1039/d3se00886j

rsc.li/sustainable-energy

Charge carrier dynamics studies of $SrTiO_3$ under applied bias offer the opportunity to gain unique insights into what underpins its state-of-the-art photocatalytic water splitting activity. Herein, time resolved spectroscopic measurements are employed, to investigate the impact of applied bias on the transient and steady state charge carrier dynamics of $SrTiO_3$ across μs–s timescales, and simultaneously measure charge extraction kinetics. A high density of Ti^{3+} defect states in $SrTiO_3$ photoanodes are identified and associated with prevalent electron trapping into deep states, which is in competition with electron extraction and limits the photocurrent. Despite the high density of trapped electrons, an intrinsically long lifetime for photogenerated holes in $SrTiO_3$ photoanodes is observed using transient absorption spectroscopy, even in the absence of applied bias. This is important for overcoming the slow kinetics and hole accumulation associated with the water oxidation reaction, and for enabling good performance in photocatalytic systems where bias cannot be applied.

Introduction

Solar-driven water splitting to obtain molecular hydrogen offers the opportunity to produce a sustainable carbon-free fuel and circumvent the intermittency of solar energy.[1,2] Photoelectrochemical (PEC) and photocatalytic water splitting have received much attention in recent years, due to their potential to produce hydrogen fuel in an up-scalable and low-cost manner.[3,4] $SrTiO_3$ is a promising metal oxide candidate for photocatalytic water splitting, due to its tunability, resistance to photocorrosion in aqueous conditions and suitable band edge positions for catalysing the water splitting reactions.[5–8] Recently, Domen and co-workers achieved a near-unity quantum efficiency of 93% at 365 nm using a $SrTiO_3$-based photocatalyst for water splitting, demonstrating highly efficient separation of photogenerated charges and subsequent catalysis.[6] However, the charge carrier dynamics that underpin these high efficiencies are not well understood, and in particular, the role of interfacial band bending on the charge carrier dynamics is not clear. Applying an electrical bias to photoelectrodes offers the opportunity to modulate such band bending and thereby investigate its impact on the charge carrier dynamics, but such investigations on $SrTiO_3$ photoanodes have been largely absent from the literature to date.

In contrast to the state-of-the-art performance of $SrTiO_3$-based photocatalysts achieving up to near-unity quantum efficiencies,[6,7,9] the performance of $SrTiO_3$ photoanodes employed in PEC water splitting are modest compared to alternative metal oxide materials. As such, research into the use of $SrTiO_3$ for water splitting has largely been focused on the use of particles for photocatalytic applications.[6,7,10–12] Following the optimisation of Nb doping to improve the conductivity and photocurrent densities of $SrTiO_3$, photocurrents of ~0.1 mA cm^{-2} have been reported.[13,14] These photocurrent are significantly lower than the photocurrents of 2.6–6.75 mA cm^{-2} achieved by photoanodes based on TiO_2, $BiVO_4$, WO_3 or α-Fe_2O_3.[15–21] Most previous work on $SrTiO_3$ photoanodes has focused on enhancing the achievable current densities, such as by doping. However, as demonstrated recently by Chen *et al.*,[22] studying the charge carrier dynamics of $SrTiO_3$ photoanodes offers valuable opportunities to investigate the impact of applied bias on the charge carrier kinetics and interfacial charge carrier processes of this material, even in the absence of high photocurrent densities. Thus, such studies can provide functional insights that would be challenging to obtain through the study of isolated particulate photocatalysts.

As is the case for many metal oxide materials, under ambient conditions $SrTiO_3$ is non-stoichiometric, with oxygen vacancies (V_O) resulting in its n-type character. In $SrTiO_3$, the formation of Ti^{3+} defect states is reported to coincide with V_O generation, in

[a]*Department of Chemistry, Centre for Processable Electronics, Imperial College London, London, W12 0BZ, UK. E-mail: j.durrant@imperial.ac.uk*

[b]*Stephenson Institute for Renewable Energy, Department of Physics, University of Liverpool, Liverpool, L69 7ZF, UK*

[c]*London Centre for Nanotechnology, Imperial College London, SW7 2AZ, UK*

[d]*School of Physics, Engineering & Technology, University of York, Heslington, York, YO10 5DD, UK*

[e]*SPECIFIC IKC, College of Engineering, Swansea University, Swansea, SA2 7AX, UK*

† Electronic supplementary information (ESI) available. See DOI: https://doi.org/10.1039/d3se00886j

order to maintain charge neutrality.[11,23] The impacts of V_O and associated defect states in metal oxides are extensive, with implications on charge trapping, recombination, transport and the resulting water splitting performance.[24–26] In order to understand the impact of these defect states, kinetic studies are often required to determine whether they enhance or are of detriment to charge separation and lifetimes.

In this work, $SrTiO_3$ photoanodes are characterised and investigated with and without applied bias, with the aim of improving our understanding of their underlying charge carrier dynamics and photophysical properties, rather than their photoanode performance. Transient absorption spectroscopy (TAS) on μs–s timescales is employed to measure the decay kinetics across the visible to NIR, in addition to the effects of bias induced band bending on charge separation and lifetimes. The application of bias to the TAS measurements enables spectral assignments to be made that do not rely on the reactivity of photogenerated charges towards chemical scavengers.[27,28] Furthermore, the charge extraction kinetics following laser excitation are determined by transient photocurrent (TPC) measurements. The combination of these characterisation techniques reveals the competition between deep electron trapping and electron extraction, which consequently limits the photocurrent densities achieved. However, even in the presence of prevalent deep electron trapping, long lived hole species are observed that are not dependent on an anodic bias, which is favourable for the use of $SrTiO_3$ in particulate photocatalysts.

Experimental

Fabrication of $SrTiO_3$ films

Transparent thin films of $SrTiO_3$ on SnO_2:F (FTO) substrates were fabricated using a radio frequency (RF) magnetron sputtering method. FTO coated substrates (TEC10, NSG Ltd) were scrubbed with Hellmanex III detergent before rinsing in ultrasonic baths of DI water and isopropyl alcohol in sequence. The $SrTiO_3$ films were deposited *via* RF magnetron sputtering from a compound target in an AJA Orion 8 sputtering system. Films were sputtered at room temperature, in a 3 mTorr Ar atmosphere and using a power density of 2.47 W cm^{-2}. Following a 10 hour deposition time, the $SrTiO_3$ films were annealed for 30 minutes in air at 450 °C.

Materials characterisation

Scanning electron microscopy (SEM) was conducted with a Leo Gemini 1525 Field Emission Gun for imaging the cross-sectional morphology of the films, sputtered with a 15 nm Cr layer. The surface topography was analysed by atomic force microscopy (AFM), using an Agilent Technologies Keysight 5500 microscope in tapping mode and with a peak amplitude voltage of 5 V. X-ray diffraction (XRD) patterns were obtained with a Bruker D2 phaser with parallel beam optics equipped with a PSD LynxEye silicon strip detector, using a Cu X-ray source (V = 30 kV, I = 10 mA) with Cu $K_{\alpha 1}$ (λ = 1.54056 Å) and Cu $K_{\alpha 2}$ radiation (λ = 1.54439 Å) emitted with an intensity ratio of 2 : 1. The ground state optical absorption was measured with a UV-vis spectrometer (Shimadzu UV-2600). The surface chemical composition and valence band structure was measured by X-ray photoelectron spectroscopy (XPS), using a Thermo K-Alpha spectrometer with a monochromated Al Kα radiation source.

Photoelectrochemical measurements

For all PEC measurements a homemade PEEK cell with quartz windows (0.5 cm^2) was employed. Here, the $SrTiO_3$ served as a photoanode (illuminated from the front side), with a Pt mesh counter electrode and Ag/AgCl in saturated KCl solution as the reference electrode. All electrodes were submerged in 0.1 M NaOH (pH 13) solution as the electrolyte. The applied bias was converted from $V_{Ag/AgCl}$ to V_{RHE} using the Nernst equation:

$$V_{RHE} = V_{Ag/AgCl} + 0.0591pH + V^0_{Ag/AgCl} \quad (1)$$

where $V^0_{Ag/AgCl}$ is the standard potential of the Ag/AgCl in saturated KCl solution reference electrode.

Microsecond transient absorption and transient photocurrent measurements

Transient absorption spectroscopy (TAS) on μs–s timescales was conducted on a home build set-up for measuring the optical signal in transmission mode. A 100 W Bentham IL1 quartz halogen lamp served as the probe light source, followed by long pass filters (Thorlabs) selected for the desired probe wavelength and an IR filter (H_2O, 5 cm path length) to prevent sample heating. The excitation source was the third harmonic of a Nd:YAG laser (Big Sky ULTRA, 8 ns pulse width, λ_{ex} = 355 nm). A liquid light guide (0.5 cm diameter) directed the laser light onto the sample. Following the sample was a was a series of lenses and mirrors for concentrating and directing the transmitted light through a motorised colour wheel (Thorlabs), followed by a monochromator (Oriel Cornerstone 130) set to the probe wavelength and finally onto a silicon photodiode detector (Hamamatsu S3071). Data at early times (ms–1 ms) was electronically amplified (Costronics) before being recorded by the oscilloscope (Tektronics DPO3012), whilst data at later times (>1 ms) was recorded by a data acquisition (DAQ) card. The two data sets were stitched together to produce a continuous transient decay across the full timescale recorded. The effects of photoluminescence and scattering from the probe light were corrected for by subtracting the data obtained in the absence of the probe light. LabVIEW software was used for data acquisition. Measurements were undertaken with the sample in a quartz cuvette, or when applying a constant bias, in a PEC cell (set up analogously to in the PEC measurements) connected to a potentiostat.

Transient photocurrent (TPC) measurements were undertaken using the same experimental set-up as for TAS measurements under applied bias, but with a change in the time base recorded by the oscilloscope. Following laser excitation with the laser pulse, the photogenerated TPC was obtained by measuring the voltage change with the oscilloscope from 10 μs to 0.1 s, triggered by the laser pulse induced trigger signal measured by

the photodiode. In this measurement, data from the DAQ is not required.

Photoinduced absorption spectroscopy

Photoinduced absorption spectroscopy (PIAS) employed the same experimental set-up as the TAS measurements, with the following modifications. Instead of the laser source, the excitation source was a 365 nm LED connected to a power supply (QL564P, Thurlby Thandar Instruments) to control the light intensity, and a MOSFET transistor (STF8NM50N, STMicroelectronics) to generate light pulses of a defined length. In this case, data from the DAQ was recorded and data from the oscilloscope is not required.

Calculation of extinction coefficient

The correlation between hole absorbance and surface hole density is used to extract the extinction coefficient (ε_{h^+}) of holes, following a method previously used in our group.[29–31] The hole absorbance was obtained from the change in optical density (ΔOD) probed at 500 nm (assumed to correspond predominantly to holes), measured by TAS measurements. The surface hole density was obtained from the cumulative charge extracted in TPC measurements, assuming that every photogenerated electron extracted results in one surface hole. This assumption was made based on a sufficiently positive bias being applied (1.3 V_{RHE}), such that back electron–hole recombination is assumed to be turned off. The charge extracted (C) was converted to surface hole density ($|h^+|$) using eqn (2):

$$|h^+| = \frac{C}{e \times A_v \times V} \quad (2)$$

where e is the elementary charge (1.60×10^{-19} C), A_v is Avogadro's number (6.02×10^{23} mol) and V is the volume investigated (PEC cell window size (cm^2) × film thickness (cm)). The gradient of the linear fit on the plot of hole absorbance *vs.* $|h^+|$ was subsequently used to extract the ε_{h^+} of holes from the Beer–Lambert law equation:

$$A = \varepsilon_{h^+} \times c \times l \quad (3)$$

where A and c are taken as the hole absorbance and surface hole density respectively, and l is the sample thickness.

Kinetic analysis

The rate law analysis method was used to approximate the kinetics of hole consumption at the $SrTiO_3$ surface, specifically by determining the hole accumulation required to achieve the rate determining step. This method has been reported previously by our group.[29–31] Briefly, at a range of light intensities from a 365 nm LED, the steady state photocurrent was measured simultaneously will the steady state optical hole signal measured by PIAS. The steady state optical hole signal was converted to a surface h^+ density using the calculated extinction coefficient of 2200 M^{-1} cm^{-1}. Similarly to for the calculation of the extinction coefficient, a sufficiently positive applied bias (1.3 V_{RHE}) was applied such that back electron–hole recombination would be excluded in the analysis and the photocurrent could be equated to the hole flux to the surface. On a log–log plot of the photocurrent *vs.* the surface hole density, the gradient can be extracted to obtain the order of reaction representing the number of accumulated hole species required to achieve the rate determining step of their consumption.

$$\tau = \frac{[\text{oxidising equivalent}]}{\text{number of electrons} \times s^{-1}} \quad (4)$$

Results

The $SrTiO_3$ photoanodes employed in this study were fabricated by RF sputtering, resulting in dense thin films on FTO coated glass substrates. The thin films had an average thickness of ~300 nm and a relatively flat surface with a roughness factor of 1.1 (Fig. 1a and S1†). Diffraction patterns obtained by XRD exhibit the expected patterns from $SrTiO_3$ (cubic perovskite) and the underlying FTO (tetragonal cassiterite) (Fig. S2†). The optical properties of the films measured by UV-vis spectroscopy demonstrate the highly transmissive nature of the films (Fig. S3a†), making them suitable for measuring TAS in transmission mode. The optical band gap obtained from Tauc plots yields an indirect band gap of ~3.3–3.4 eV (Fig. S3b†). Although this is marginally larger than that typically reported for bulk $SrTiO_3$ (~3.2 eV),[23,32,33] this is typical of thin $SrTiO_3$ films fabricated by RF sputtering.[34,35] The chemical composition measured by XPS reveals a relative contribution of Ti^{3+} defect states of 4% compared to Ti^{4+} states (Fig. 1b), and the valence XPS indicates a E_F position that is approximately 2 eV above the valence band (Fig. S4†). The current–voltage response of the $SrTiO_3$ photoanode was measured under chopped light conditions (Fig. S5†). The onset potential for photocurrent generation of 0.4 V_{RHE} is in good agreement with that reported previously.[14] As the potential increases further, the photocurrent increases and reaches a modest 7 μA cm^{-2} at 1.23 V_{RHE}, consistent with the low photocurrents expected for unmodified $SrTiO_3$.[13,14]

The charge carrier dynamics of the $SrTiO_3$ films were first investigated in the absence of applied bias and under inert N_2 conditions. The transient absorption spectrum at 10 μs is comprised of two features: a feature in the visible (<600 nm) that grows in amplitude with decreasing wavelengths and a broad feature in the early-NIR (Fig. 2a). Such features in the visible and early-NIR regions are in good agreement with the spectroscopic features reported in the literature on μs timescales for $SrTiO_3$ particulate photocatalysts, and vary in relative intensity depending on the fabrication route and defects present.[36,37] The decay kinetics exhibit a clear dependence on probe wavelength, with a distinct change in decay kinetics observed at probe wavelengths below and above 600 nm (Fig. 2b). Interestingly, the lifetimes observed below 600 nm are much longer than those typically observed in metal oxides in the absence of bias or chemical scavengers.[27,28,38]

The impact of applied bias on the decay kinetics was investigated, to enable spectral assignments of the two spectral features with distinct decay kinetics, as well as to determine the

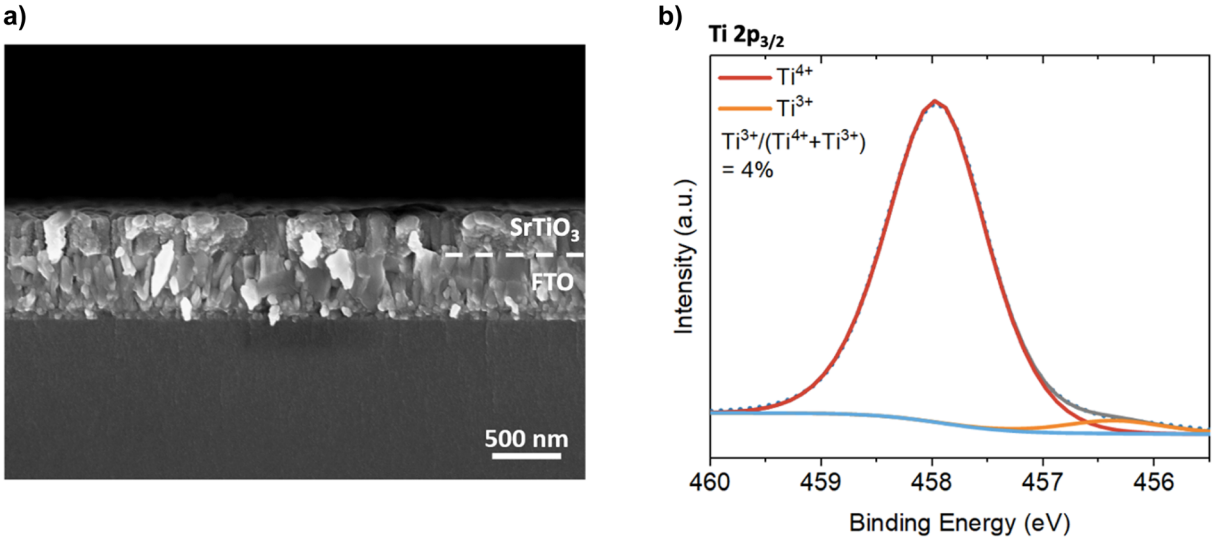

Fig. 1 (a) Side on SEM image of the polycrystalline $SrTiO_3$ film on FTO, showing a dense film with an average thickness of ~300 nm on top of the FTO layer. (b) XPS Ti 2p core line spectrum, fitted for the Ti $2p_{3/2}$ peak and showing a relative Ti^{3+} contribution of 4%.

role of applied bias in modulating band bending and the resulting charge carrier dynamics. With increasingly anodic bias, electron extraction is increased (as observed as an increase in photocurrent, Fig. S5†) and is therefore expected to increase the yield of long lived holes. At 500 nm, the decay kinetics become slower and the optical signals increase in amplitude with increasingly anodic bias (Fig. 3a). Thus, 500 nm and the corresponding spectral region probed below 600 nm is assigned primarily to hole species. In contrast, at 800 nm the decay kinetics accelerate and optical signals decrease in amplitude with increasingly anodic bias (Fig. 3b). Therefore, 800 nm and the corresponding early-NIR feature is assigned primarily to electron species. This distinction between photoinduced absorption in the visible and NIR spectral regions being preferentially dominated by respectively hole and electron absorption is typical of $SrTiO_3$ and other metal oxides.[36,37,39–42] Although this bias dependence of the decay kinetics was sufficient to make spectral assignments, the bias dependence was much less dramatic than that observed in other metal oxides.[27,28,38] This is consistent with the low photocurrent densities and suggests that factors other than bias induced band bending are responsible for the long hole lifetimes. The distinct kinetics observed for holes and electrons suggests that the decays observed do not simply correspond to the recombination of the two probed species. Instead, an additional decay pathway that reduces electron lifetimes must be present. As such, our observation of faster electron decays compared to hole decays, even at modest anodic biases where no photocurrent is observed, indicates two competing processing for electron decay on the timescales studied: electron relaxation/trapping within the $SrTiO_3$ and, under strong anodic bias, electron extraction to the external circuit. The immobile nature of trapped charges may also contribute to the small degree of bias dependence, as explored further in the discussion.

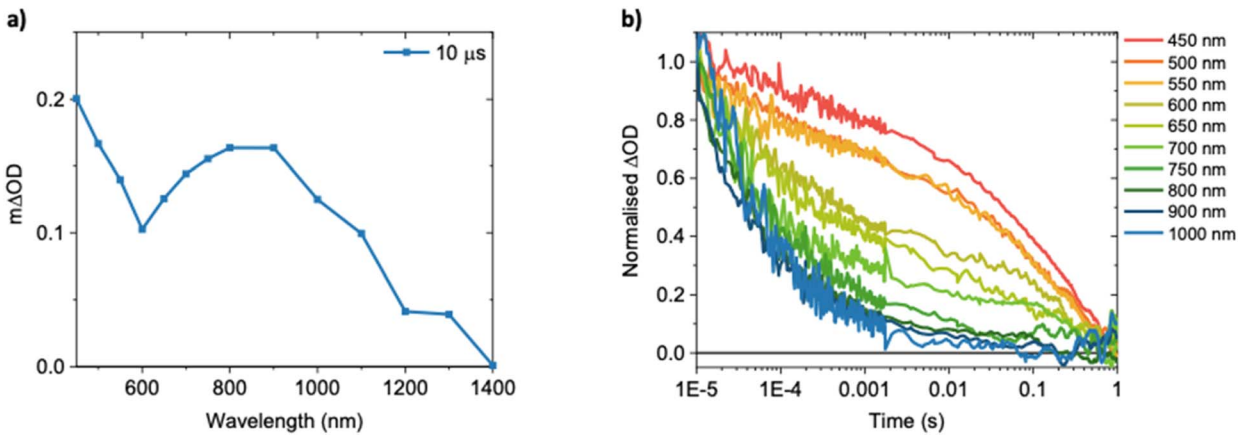

Fig. 2 TAS measurements of a $SrTiO_3$ photoanode in N_2 (no electrolyte) using a 355 nm laser at an excitation intensity of 400 μJ cm^{-2} and 0.8 Hz repetition rate. (a) TAS spectrum measured at 10 μs. (b) Normalised decay kinetics measured across the spectral range.

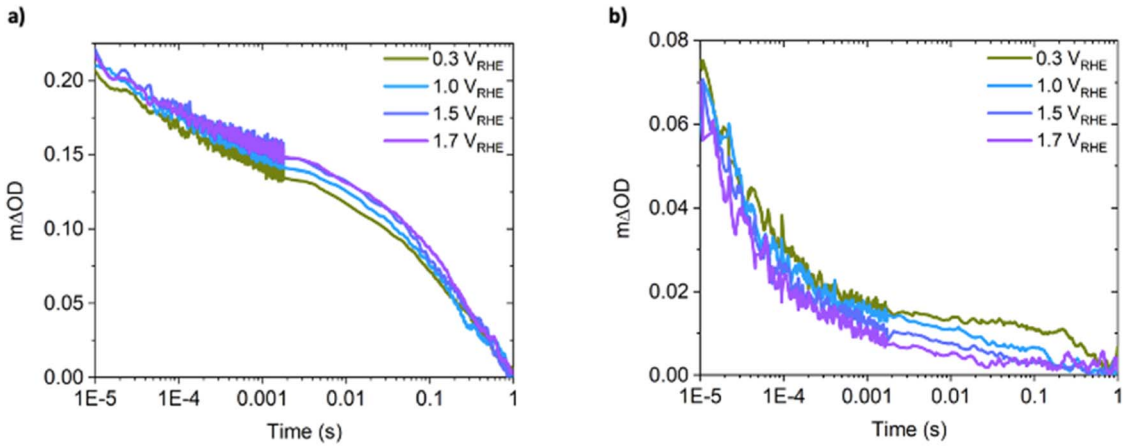

Fig. 3 $SrTiO_3$ photoanode TAS decays in 0.1 M NaOH under applied bias, using a 355 nm laser at an excitation intensity of 400 μJ cm^{-2} and 0.8 Hz repetition rate. Probed at (a) 500 nm, and (b) 800 nm.

The charge extraction kinetics from TPC measurements, undertaken in parallel with the TAS experiments, show reasonably fast kinetics, with a peak charge extraction at 0.1 ms (Fig. 4a). These kinetics are similar to those observed in $BiVO_4$ photoanodes, and significantly faster than in WO_3.[26,38] These charge extraction kinetics are also consistent with the timescales at which the TAS electron signal exhibits accelerated decays with increasingly anodic applied bias (Fig. 3b) (*i.e.*: only a marginal fractional change in the TAS electron signal is observed at 10 μs with anodic bias, but there is increasing signal loss at longer time delays). This confirms that the faster electron decays at strong anodic bias can be assigned to increased electron extraction.

Using the cumulative charge extracted (Fig. 4b) and the earlier spectral assignment of holes, the hole extinction coefficient (ε_{h^+}) can be calculated using a method previously reported in our group and explained in the Experimental section.[29–31] Briefly, this method uses the Beer–Lambert law and the relationship between the hole absorbance (measured in TAS at 500 nm, Fig. 4c) and the surface hole density (calculated from the cumulative charge extracted, Fig. 4b) at a range of excitation intensities, to extract the ε_{h^+}. The TAS and TPC measurements used to extract the hole absorbance and surface hole density are undertaken under a sufficiently anodic applied bias (1.3 V_{RHE}), whereby the absence of photocurrent spikes in Fig. S5 and S6a† suggests back electron–hole recombination has been turned off. Both the hole absorbance and surface hole density increase with increasing excitation intensities, until they begin to plateau at 630 μJ cm^{-2}. It is notable that the decay dynamics of this TAS hole signal are independent of laser intensity, indicating that the decays do not result from bimolecular recombination, which is consistent with our conclusion above regarding the decay kinetics not simply being the result of recombination of the probed species. Instead, the decays are attributed to a monomolecular process, as we discuss further below. A linear correlation between the hole absorbance and surface hole density is obtained (Fig. 4d). The ε_{h^+} is subsequently extracted from the gradient of the linear fit using the Beer–Lambert law, to yield a ε_{h^+} of 2200 ± 100 M^{-1} cm^{-1}. Since this is the first calculation of the ε_{h^+} in $SrTiO_3$ to our knowledge, it cannot be compared to previously reported values for $SrTiO_3$. However, it is reasonable when compared to the ε_{h^+} reported for dense anatase TiO_2, of 2000–2930 M^{-1} cm^{-1},[30,43] which has similar optoelectronic properties to $SrTiO_3$, such as valence and conduction bands that correspond to the density of states from O 2p and Ti 3d orbitals respectively.[44] It is noted that despite the reasonable ε_{h^+} value and associated error, the linear fit does not completely extrapolate to zero, suggesting that there is a small electron contribution to the 500 nm absorbance.

The steady-state kinetics of hole accumulation and decay were measured by PIAS using a quasi-steady state 8 second LED light pulse under strong anodic bias. The PIAS signals increase with increasing excitation intensities (Fig. 5), which is attributed to increased charge generation and resulting steady-state charge densities. Upon light-off, the hole signals decay with $t_{50\%}$ decay times of ~0.5 s (Fig. 5, inset). These hole decays, which most likely have contributions from recombination and water oxidation, are termed τ_{dec} herein. Following this initial decay there is a residual signal that remains and decays very slowly, likely due to a population of trapped hole species that do not contribute to photoelectrochemical activity.[45–47] The kinetics of hole consumption were further investigated by a rate law analysis, where the hole flux to the surface (equated to the photocurrent extracted) is correlated to the steady-state surface hole density.[29–31,48–50] To achieve this, the steady-state photocurrent (Fig. S6a†) is measured simultaneously with the steady-state hole absorbance in PIAS (Fig. 5). The hole absorbance signal is converted to a surface hole density, using the calculated hole extinction coefficient of 2200 M^{-1} cm^{-1} (Fig. 4d). Under these conditions a second order reaction is measured (Fig. S6b†), in agreement with a recent study by Chen *et al.*,[22] and previously reported orders between one and three for other metal oxide photoanodes.[29–31] A second order reaction indicates that the rate limiting step of water oxidation, on $SrTiO_3$ photoanodes under these operating conditions, involves the accumulation of two hole species (or oxidising equivalents).

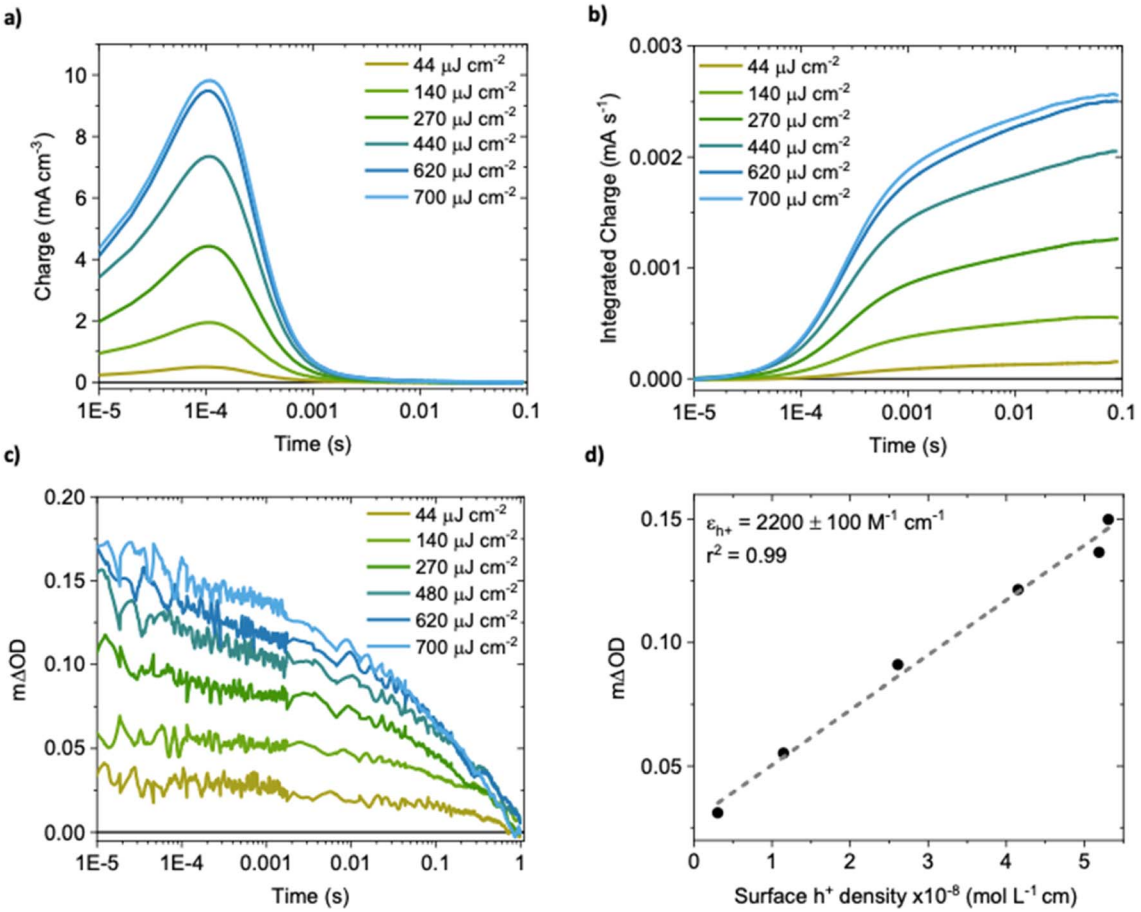

Fig. 4 Measurements undertaken on a $SrTiO_3$ photoanode under an applied bias of 1.3 V_{RHE} in 0.1 M NaOH and with increasing laser excitation intensities for the calculation of the ε_{h^+}, using a 355 nm laser at a 0.8 Hz repetition rate. (a) TPC measured as the charge extracted as a function of time following laser excitation. (b) The integrated charge extracted from the TPC in (a). (c) TAS decays probed at 500 nm. (d) Plot of the hole absorbance measured by TAS *vs.* the surface hole density calculated from the charge extracted, with the ε_{h^+} obtained from the gradient of the linear fit.

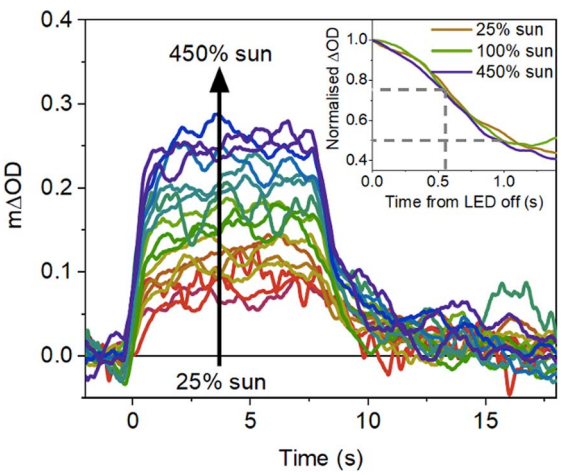

Fig. 5 PIAS traces probed at 500 nm, under an applied bias of 1.3 V_{RHE} in 0.1 M NaOH and with increasing LED excitation intensities. Decay kinetics are shown in the inset, including extrapolation to yield the $t_{50\%}$ time of the decay (~0.5 s).

However, due to the low photocurrent densities observed herein, we are cautious of strongly assigning hole consumption to water oxidation alone. The reaction time constant can also be calculated from the ratio between the hole flux to the surface and the surface hole density (Fig. S7†). The hole decay times indicated by this time constant only take into account the reaction of surface holes that have avoided electron–hole recombination and are termed τ_{surf}. The τ_{surf} values calculated are in the range of 1–5 s, which indicates a slower hole decay time than that obtained from the PIAS decays (0.15–0.5 s). This is consistent with τ_{surf} being indicative of water oxidation kinetics alone, whilst τ_{dec} results from the sum of both water oxidation and hole recombination/trapping pathways, which will be explored further in the discussion.

Discussion

Herein, the charge carrier dynamics of $SrTiO_3$ photoanodes are investigated with and without applied bias. Impressively, long hole lifetimes are observed that do not rely on applied bias, and are even observed in bias free conditions. This is unusual for

metal oxide photoanodes and implies that bias induced band bending is not required to achieve long charge carrier lifetimes in $SrTiO_3$. However, the photocurrents achieved herein are comparatively low. Given that the rate of electron extraction is reasonably fast, other factors, such as electron trapping,[26] must be responsible for the low photocurrent, and are discussed further in this section.

Using TAS on μs–s timescales, distinctly different decay kinetics of electrons and holes are observed, with slower decay kinetics attributed to the hole species probed below ~600 nm. This is indicative of an additional decay pathway being present that extends hole lifetimes. Interestingly, wavelength dependent decay kinetics and long lifetimes in the absence of applied bias have also been observed in $BaTiO_3$,[51] which shares the cubic perovskite structure of $SrTiO_3$. Even though the bias dependence of the TAS kinetics was sufficiently clear to enable confident spectral assignments and calculation of the ε_{h^+}, the extent of changes in TAS signals with bias dependence was small compared to what is commonly observed in other metal oxide photoanodes.[27,28,30,52] The small degree of bias dependence in $SrTiO_3$ and considerable charge carrier lifetimes, even in the absence of bias, implies that the intrinsic properties of $SrTiO_3$ enable the generation of remarkably long lived holes. This is an especially important feature in photocatalytic applications of $SrTiO_3$ particles, where a bias cannot be applied to drive the necessary charge separation and lifetime gains for the slow interfacial water splitting reactions.

The chemical doping density from Ti^{3+} donor states, that are associated with electron occupied oxygen vacancies and approximated using the Ti^{3+} concentration measured by XPS, is high at $\sim 10^{20}$ cm^{-3}. The high Ti^{3+} chemical doping density is indicative of a high electron occupancy of the Ti^{3+} defect states, suggesting that they are sufficiently deep to have much of their distribution below the E_F level. The deeply trapped electrons in these states are likely to be immobile and unable to be extracted to contribute to the photocurrent. Thus, the prevalent trapping of electrons into deep V_O states, prior to the timescales of the TAS measurement, may explain the low photocurrents measured herein, despite the relatively fast electron carrier extraction rate (peaking at 0.1 ms) and intrinsic charge separation properties in $SrTiO_3$ observed. With this in mind, the improved photocatalytic performance of Al^{3+} doped $SrTiO_3$,[8] likely results from the suppression of these deep trap states. The large Ti^{3+} chemical doping density is approaching that of WO_3 ($\sim 10^{20}$–10^{22} cm^{-3}),[53,54] which is widely recognised for its high doping density from V_O, that result in W^{5+} states when occupied by an electron.[41] In WO_3, a slow charge extraction rate (peaking at 1 ms)[38] coincides with the high density of V_O, due to the slow trapping–detrapping electron transport that proceeds *via* the shallow trap states.[25] In $SrTiO_3$, the electron trapping may limit the size of the photocurrent but it does not result in a slow extraction rate, possibly due to the immobile nature of the deeply trapped electrons limiting their influence on the charge extraction kinetics.[55] The immobile nature of these trapped charges also aids explanation of the small degree of bias dependence of the decay kinetics.

The τ_{dec} extracted from the PIAS decays (~0.5 s) is shorter than the τ_{surf} calculated using the comparison of the accumulated hole density *vs.* the photocurrent density (1–5 s). The τ_{surf} only takes into account the reaction of surface holes with the electrolyte (*i.e.* water oxidation), whereas the PIAS decay times, τ_{dec}, are determined by the sum of recombination and water oxidation kinetics. Thus, the faster τ_{dec} times measured by PIAS suggests that even under strongly anodic bias, there is significant competition between water oxidation and an additional decay pathway for long lived holes. This additional decay pathway is attributed to electron–hole recombination mediated by the prevalent electron trapping into deep Ti^{3+} states, and is consistent with the excitation density independent hole decays measured in Fig. 4c. With this in mind the τ_{surf} could be accelerated by material modifications, for example by adding a co-catalyst that promotes the water oxidation reaction, as has been reported previously.[56,57] Cuk and co-workers previously reported the formation of intermediate Ti–O˙ surface radical species on $SrTiO_3$, and suggested that holes were trapped as these surface radical sites on ps timescales.[58] It is likely that the long lived holes we observe herein correspond to such Ti–O˙ radicals, with our data indicating that spatial separation from Ti^{3+} states enables their long lifetimes and a significant fraction of these to remain for 0.5 s after photogeneration. As discussed above, our PIAS data indicate that water oxidation by these $SrTiO_3$ surface radicals proceeds on the 1–5 s timescale, slightly slower than the typical timescales of water oxidation on other metal oxides such as TiO_2 at low surface hole densities.[30] These slower kinetics may in part be related to the relatively low densities of surface holes accumulating on our electrodes due to competing recombination/trapping pathways.

It is striking that despite the high defect densities we identified in these $SrTiO_3$ photoanodes, we also observed remarkably long lived holes (possibly as surface Ti–O˙ radicals), even in the absence of anodic bias. In particular, it is noteworthy that the high density ($\sim 10^{20}$ cm^{-3}) of Ti^{3+} states do not result in rapid hole recombination. This may be associated with the unusually high dielectric constant of $SrTiO_3$ compared to other oxides (~300 for $SrTiO_3$,[59–62] compared to 13–45 for anatase TiO_2,[63] 32–86 for $BiVO_4$,[64–66] and 18–26 for α-Fe_2O_3 (ref. 67 and 68)), which can be expected to reduce the Coulomb attraction of electrons and holes. It is also possible that band bending resulting from surface dipoles between facets of differing energy may aid the spatial separation of these holes from Ti^{3+} states.[69,70] An energy offset between facets with different surface dipoles was previously proposed as the reason for facet selective photodeposition of co-catalysts on the near-unity $SrTiO_3$ photocatalyst materials.[6] In either case, the ability of $SrTiO_3$ to sustain these long hole lifetimes is likely to be a key factor behind the success of this material in photocatalyst particles for unassisted water splitting.[6,7,9]

The charge carrier dynamics of our $SrTiO_3$ photoanodes obtained herein, using TAS on μs–s timescales, PIAS and TPC measurements, are summarised in Fig. 6. As observed in the TAS data in Fig. 3b, electron trapping occurs on the <0.1 ms timescale, most likely resulting from the formation of localised Ti^{3+} states associated with the deep V_O states. As a result of this

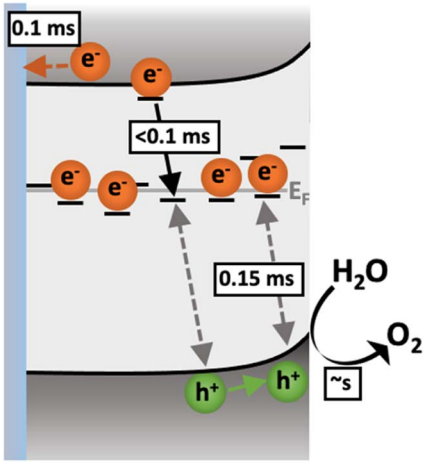

Fig. 6 Schematic illustration of the operation of the $SrTiO_3$ photoanode under strong anodic applied bias, where back electron–hole recombination is assumed to be turned off. Timescales in white boxes are that of electron extraction, trapping, and water oxidation processes, as indicated by TPC, TAS and PIAS measurements. Electrons are extracted on competing timescales (~0.1 ms) of electron trapping into deep Ti^{3+} states (<0.1 ms). Water oxidation is slow and occurs on second timescales, in kinetic competition with faster (0.15–0.5 s) back electron hole recombination.

deep trapping, a significant population of the electrons are relatively immobile, and therefore cannot be efficiently extracted. This electron trapping appears to be in kinetic competition with electron extraction to the external circuit on the ~0.1 ms timescale. This electron trapping, and bulk recombination losses from the high density of Ti^{3+} states, appear to be the primary origins of the low photocurrent densities observed for these photoanodes. As a result of prevalent charge trapping and recombination in the $SrTiO_3$ herein, even under anodic bias, the hole densities that accumulate in $SrTiO_3$ on long (ms–s) timescales are low. Surface holes (Ti–O$^{\bullet}$ radicals) oxidise water on seconds timescales, in competition with faster (0.15–0.5 s) recombination losses, most likely associated with back electron–hole recombination with Ti^{3+} states. The ability of $SrTiO_3$ to maintain long hole lifetimes regardless of the applied bias is remarkable and aids explanation of why $SrTiO_3$ is well suited to particulate photocatalytic applications despite its low photocurrents.

Conclusions

In this work, the charge carrier dynamics of photogenerated charges in a $SrTiO_3$ photoanode under applied bias were investigated for the first time. Even though $SrTiO_3$ is not the highest performing photoanode material, the insights gained herein highlight its suitability for particulate photocatalytic water splitting applications. On slow timescales (μs–s), holes exhibit remarkably long lifetimes, which is advantageous when considering the slow kinetics and hole accumulation associated with the water oxidation reaction. The intrinsic ability of $SrTiO_3$ to sustain long hole lifetimes regardless of applied bias is demonstrated, which is integral for its application in particulate photocatalytic water splitting, where a bias cannot be applied to drive charge carrier separation. However, we find that despite the long lived holes observed, the photocurrent of the $SrTiO_3$ photoanodes is greatly limited by the competition between deep electron trapping and electron extraction. Thus, it is important to suppress the deep Ti^{3+} states that trap electrons to achieve improved photoanode performance, in line with the recognised role of Al^{3+} in improving $SrTiO_3$ photocatalyst performance.

Conflicts of interest

There are no conflicts to declare.

Acknowledgements

A. W. thanks the EPSRC for DTP funding. J. R. D. thanks the EPSRC ATIP project (EP/TO28513/1) for funding. Professor Kazunari Domen and Professor Takashi Hisatomi from Shinshu University, and Dr Benjamin Moss from Imperial College London, are thanked for useful discussions. A. K. thanks the EPSRC for a Programme Grant (EP/W017075/1) and the Royal Society for an Equipment Grant (RSG\R1\180434). T. P. S. thanks the EPSRC for funding (EP/W03445X/1). A. M. thanks the EPSRC for funding (EP/L01551X/1).

Notes and references

1 Q. Wang and K. Domen, *Chem. Rev.*, 2020, **120**, 919–985.
2 B. Moss, O. Babacan, A. Kafizas and A. Hankin, *Adv. Energy Mater.*, 2021, **11**, 1–43.
3 B. A. Pinaud, J. D. Benck, L. C. Seitz, A. J. Forman, Z. Chen, T. G. Deutsch, B. D. James, K. N. Baum, G. N. Baum, S. Ardo, H. Wang, E. Miller and T. F. Jaramillo, *Energy Environ. Sci.*, 2013, **6**, 1983–2002.
4 S. Chen, T. Takata and K. Domen, *Nat. Rev. Mater.*, 2017, **2**, 1–17.
5 A. Kudo and Y. Miseki, *Chem. Soc. Rev.*, 2009, **38**, 253–278.
6 T. Takata, J. Jiang, Y. Sakata, M. Nakabayashi, N. Shibata, V. Nandal, K. Seki, T. Hisatomi and K. Domen, *Nature*, 2020, **581**, 411–414.
7 Y. Goto, T. Hisatomi, Q. Wang, T. Higashi, K. Ishikiriyama, T. Maeda, Y. Sakata, S. Okunaka, H. Tokudome, M. Katayama, S. Akiyama, H. Nishiyama, Y. Inoue, T. Takewaki, T. Setoyama, T. Minegishi, T. Takata, T. Yamada and K. Domen, *Joule*, 2018, **2**, 509–520.
8 Y. Ham, T. Hisatomi, Y. Goto, Y. Moriya, Y. Sakata, A. Yamakata, J. Kubota and K. Domen, *J. Mater. Chem. A*, 2016, **4**, 3027–3033.
9 Q. Wang, T. Hisatomi, Q. Jia, H. Tokudome, M. Zhong, C. Wang, Z. Pan, T. Takata, M. Nakabayashi, N. Shibata, Y. Li, I. D. Sharp, A. Kudo, T. Yamada and K. Domen, *Nat. Mater.*, 2016, **15**, 611–615.
10 T. Minegishi, H. Nishiyama, T. Hisatomi, M. Yoshida, H. Lyu, M. Katayama, K. Domen, Y. Goto, K. Asakura, Y. Sakata, T. Yamada, T. Higashi and T. Takata, *Chem. Sci.*, 2019, **10**, 3196–3201.

11 Z. Zhao, R. V. Goncalves, S. K. Barman, E. J. Willard, E. Byle, R. Perry, Z. Wu, M. N. Huda, A. J. Moulé and F. E. Osterloh, *Energy Environ. Sci.*, 2019, **12**, 1385–1395.
12 Q. Wang, T. Hisatomi, Q. Jia, H. Tokudome, M. Zhong, C. Wang, Z. Pan, T. Takata, M. Nakabayashi, N. Shibata, Y. Li, I. D. Sharp, A. Kudo, T. Yamada and K. Domen, *Nat. Mater.*, 2016, **15**, 611–615.
13 A. N. Pinheiro, E. G. S. Firmiano, A. C. Rabelo, C. J. Dalmaschio and E. R. Leite, *RSC Adv.*, 2014, **4**, 2029–2036.
14 S. Kawasaki, R. Takahashi and M. Lippmaa, *J. Phys. Chem. C*, 2019, **123**, 15551–15556.
15 T. W. Kim, Y. Ping, G. A. Galli and K. S. Choi, *Nat. Commun.*, 2015, **6**, 1–10.
16 J. Y. Kim, G. Magesh, D. H. Youn, J. W. Jang, J. Kubota, K. Domen and J. S. Lee, *Sci. Rep.*, 2013, **3**, 1–8.
17 J. K. Kim, K. Shin, S. M. Cho, T. W. Lee and J. H. Park, *Energy Environ. Sci.*, 2011, **4**, 1465–1470.
18 J. S. Yang, W. P. Liao and J. J. Wu, *ACS Appl. Mater. Interfaces*, 2013, **5**, 7425–7431.
19 Z. Wang, X. Huang and X. Wang, *Catal. Today*, 2019, **335**, 31–38.
20 M. Liu, N. D. L. Snapp and H. Park, *Chem. Sci.*, 2011, **2**, 80–87.
21 Y. Pihosh, I. Turkevych, K. Mawatari, J. Uemura, Y. Kazoe, S. Kosar, K. Makita, T. Sugaya, T. Matsui, D. Fujita, M. Tosa, M. Kondo and T. Kitamori, *Sci. Rep.*, 2015, **5**, 1–2.
22 R. Chen, D. Zhang, Z. Wang, D. Li, L. Zhang, X. Wang, F. Fan and C. Li, *J. Am. Chem. Soc.*, 2023, **145**, 4667–4674.
23 T. Takata and K. Domen, *J. Phys. Chem. C*, 2009, **113**, 19386–19388.
24 S. Corby, R. R. Rao, L. Steier and J. R. Durrant, *Nat. Rev. Mater.*, 2021, **6**, 1136–1155.
25 S. Corby, L. Francás, A. Kafizas, J. R. Durrant, L. Francàs, A. Kafizas and J. R. Durrant, *Chem. Sci.*, 2020, **11**, 2907–2914.
26 S. Selim, E. Pastor, M. García-Tecedor, M. R. Morris, L. Francàs, M. Sachs, B. Moss, S. Corby, C. A. Mesa, S. Gimenez, A. Kafizas, A. A. Bakulin and J. R. Durrant, *J. Am. Chem. Soc.*, 2019, **141**, 18791–18798.
27 Y. Ma, S. R. Pendlebury, A. Reynal, F. Le Formal and J. R. Durrant, *Chem. Sci.*, 2014, **5**, 2964–2973.
28 S. R. Pendlebury, A. J. Cowan, M. Barroso, K. Sivula, J. Ye, M. Grätzel, D. R. Klug, J. Tang and J. R. Durrant, *Energy Environ. Sci.*, 2012, **5**, 6304–6312.
29 Y. Ma, C. A. Mesa, E. Pastor, A. Kafizas, L. Francàs, F. Le Formal, S. R. Pendlebury and J. R. Durrant, *ACS Energy Lett.*, 2016, **1**, 618–623.
30 A. Kafizas, Y. Ma, E. Pastor, S. R. Pendlebury, C. Mesa, L. Francàs, F. Le Formal, N. Noor, M. Ling, C. Sotelo-Vazquez, C. J. Carmalt, I. P. Parkin and J. R. Durrant, *ACS Catal.*, 2017, **7**, 4896–4903.
31 F. Le Formal, E. Pastor, S. D. Tilley, C. A. Mesa, S. R. Pendlebury, M. Grätzel and J. R. Durrant, *J. Am. Chem. Soc.*, 2015, **137**, 6629–6637.
32 D. Kan, T. Terashima, R. Kanda, A. Masuno, K. Tanaka, S. Chu, H. Kan, A. Ishizumi, Y. Kanemitsu, Y. Shimakawa and M. Takano, *Nat. Mater.*, 2005, **4**, 816–819.
33 Y. Yamada and Y. Kanemitsu, *Phys. Rev. B: Condens. Matter Mater. Phys.*, 2010, **82**, 1–4.
34 J. H. Ma, Z. M. Huang, X. J. Meng, S. J. Liu, X. D. Zhang, J. L. Sun, J. Q. Xue, J. H. Chu and J. Li, *J. Appl. Phys.*, 2006, **99**, 033515.
35 D. Xu, Y. Yuan, H. Zhu, L. Cheng, C. Liu, J. Su, X. Zhang, H. Zhang, X. Zhang and J. Li, *Materials*, 2019, **12**, 138.
36 A. Yamakata, H. Yeilin, M. Kawaguchi, T. Hisatomi, J. Kubota, Y. Sakata and K. Domen, *J. Photochem. Photobiol., A*, 2015, **313**, 168–175.
37 A. Yamakata, J. J. M. Vequizo and M. Kawaguchi, *J. Phys. Chem. C*, 2015, **119**, 1880–1885.
38 S. Corby, L. Francàs, S. Selim, M. Sachs, C. Blackman, A. Kafizas and J. R. Durrant, *J. Am. Chem. Soc.*, 2018, **140**, 16168–16177.
39 E. Pastor, J. S. Park, L. Steier, S. Kim, M. Grätzel, J. R. Durrant, A. Walsh and A. A. Bakulin, *Nat. Commun.*, 2019, **10**, 1–7.
40 M. Sachs, E. Pastor, A. Kafizas and J. R. Durrant, *J. Phys. Chem. Lett.*, 2016, **7**, 3742–3746.
41 M. Sachs, J. S. Park, E. Pastor, A. Kafizas, A. A. Wilson, L. Francàs, S. Gul, M. Ling, C. Blackman, J. Yano, A. Walsh and J. R. Durrant, *Chem. Sci.*, 2019, **10**, 5667–5677.
42 X. Wang, A. Kafizas, X. Li, S. J. A. Moniz, P. J. T. Reardon, J. Tang, I. P. Parkin and J. R. Durrant, *J. Phys. Chem. C*, 2015, **119**, 10439–10447.
43 A. J. Cowan, W. Leng, P. R. F. Barnes, D. R. Klug and J. R. Durrant, *Phys. Chem. Chem. Phys.*, 2013, **15**, 8772–8778.
44 M. Arai, S. Kohiki, H. Yoshikawa, S. Fukushima, Y. Waseda and M. Oku, *Phys. Rev. B: Condens. Matter Mater. Phys.*, 2002, **65**, 1–6.
45 R. Godin, T. Hisatomi, K. Domen and J. R. Durrant, *Chem. Sci.*, 2018, **9**, 7546–7555.
46 W. Yang, R. Godin, H. Kasap, B. Moss, Y. Dong, S. A. J. Hillman, L. Steier, E. Reisner and J. R. Durrant, *J. Am. Chem. Soc.*, 2019, **141**, 11219–11229.
47 C. Adler, S. Selim, I. Krivtsov, C. Li, D. Mitoraj, B. Dietzek, J. R. Durrant and R. Beranek, *Adv. Funct. Mater.*, 2021, **31**, 2105369.
48 L. Francàs, C. A. Mesa, E. Pastor, F. Le Formal and J. R. Durrant, *RSC Energy Environ. Ser.*, 2018, 128–162.
49 L. Francàs, S. Corby, S. Selim, D. Lee, C. A. Mesa, R. Godin, E. Pastor, I. E. L. Stephens, K. S. Choi and J. R. Durrant, *Nat. Commun.*, 2019, **10**, 1–10.
50 E. Pastor, F. Le Formal, M. T. Mayer, S. D. Tilley, L. Francàs, C. A. Mesa, M. Grätzel and J. R. Durrant, *Nat. Commun.*, 2017, **8**, 14280.
51 M. R. Morris, S. R. Pendlebury, J. Hong, S. Dunn and J. R. Durrant, *Adv. Mater.*, 2016, **28**, 7123–7128.
52 M. Barroso, S. R. Pendlebury, A. J. Cowan and J. R. Durrant, *Chem. Sci.*, 2013, **4**, 2724–2734.
53 X. Liu, F. Wang and Q. Wang, *Phys. Chem. Chem. Phys.*, 2012, **14**, 7894.
54 M. Regragui, V. Jousseaume, M. Addou, A. Outzourhit, J. C. Bernéde and B. El Idrissi, *Thin Solid Films*, 2001, **397**, 238–243.

55 B. Moss, H. Le, S. Corby, K. Morita, S. Selim, C. Sotelo-Vazquez, Y. Chen, A. Borthwick, A. Wilson, C. Blackman, J. R. Durrant, A. Walsh and A. Kafizas, *J. Phys. Chem. C*, 2020, **124**, 18859–18867.
56 D. Wang, R. Li, J. Zhu, J. Shi, J. Han, X. Zong and C. Li, *J. Phys. Chem. C*, 2012, **116**, 5082–5089.
57 R. Godin, A. Kafizas and J. R. Durrant, *Curr. Opin. Electrochem.*, 2017, **2**, 136–143.
58 D. M. Herlihy, M. M. Waegele, X. Chen, C. D. Pemmaraju, D. Prendergast and T. Cuk, *Nat. Chem.*, 2016, **8**, 549–555.
59 N. F. Muhamad, R. A. M. Osman, M. S. Idris and M. N. M. Yasin, *EPJ Web Conf.*, 2017, **162**, 2–5.
60 B. Pongthippitak, P. Wongtha, P. Reabroy, P. Kunsuwan and S. Thountom, *J. Phys.: Conf. Ser.*, 2018, **1144**, 012162.
61 M. Marques, L. K. Teles, V. Anjos, L. M. R. Scolfaro, J. R. Leite, V. N. Freire, G. A. Farias and E. F. Da Silva, *Appl. Phys. Lett.*, 2003, **82**, 3074–3076.
62 R. M. Doughty, B. Hodges, J. Dominguez, R. Han, Z. Zhao, S. Assavachin and F. E. Osterloh, *J. Phys. Chem. C*, 2020, **124**, 18426–18435.
63 M. Dou and C. Persson, *J. Appl. Phys.*, 2013, **113**, 083703.
64 S. Sarkar and K. K. Chattopadhyay, *Phys. E*, 2012, **44**, 1742–1746.
65 K. H. Ye, X. Yu, Z. Qiu, Y. Zhu, X. Lu and Y. Zhang, *RSC Adv.*, 2015, **5**, 34152–34156.
66 D. K. Zhong, S. Choi and D. R. Gamelin, *J. Am. Chem. Soc.*, 2011, **133**, 18370–18377.
67 R. A. Lunt, A. J. Jackson and A. Walsh, *Chem. Phys. Lett.*, 2013, **586**, 67–69.
68 O. Madelung, U. Rössler and M. Schulz, in Non-Tetrahedrally Bonded Binary Compounds II, *Landolt-Börnstein – Group III Condensed Matter*, Springer-Verlag Berlin Heidelberg, 2000.
69 L. Mu, B. Zeng, X. Tao, Y. Zhao and C. Li, *J. Phys. Chem. Lett.*, 2019, **10**, 1212–1216.
70 Y. Qi, J. Zhang, Y. Kong, Y. Zhao, S. Chen, D. Li, W. Liu, Y. Chen, T. Xie, J. Cui, C. Li, K. Domen and F. Zhang, *Nat. Commun.*, 2022, **13**, 1–9.